Article

Coprisin/Compound K Conjugated Gold Nanoparticles Induced Cell Death through Apoptosis and Ferroptosis Pathway in Adenocarcinoma Gastric Cells

Sanjeevram Dhandapani,[¶] Abdus Samad,[¶] Ying Liu, Rongbo Wang, Sri Renukadevi Balusamy, Haribalan Perumalsamy,* and Yeon-Ju Kim*

Cite This: *ACS Omega* 2024, 9, 25932−25944

Read Online

ACCESS | Metrics & More | Article Recommendations | Supporting Information

ABSTRACT: Ferroptosis and apoptosis are programmed cell death pathways with distinct characteristics. Sometimes, cancer cells are aided by the induction of a different pathway, such as ferroptosis, when they develop chemoresistance and avoid apoptosis. Identifying the nanomedicine that targets dual pathways is considered as one of the best strategies for diverse cancer types. In our previous work, we synthesized gold nanoparticles (GNP) utilizing *Gluconacetobacter liquefaciens* in conjunction with compound K (CK) and coprisin (CopA3), yielding GNP-CK-CopA3. Here, we assessed the inhibitory effect of GNP-CK-CopA3 on AGS cells and the induction of apoptosis using Hoechst and PI, Annexin V-FITC/PI, and qRT-PCR. Subsequently, we conducted downstream proteomic analysis and molecular dynamic stimulation to identify the underlying molecular mechanisms. Our investigation of cultured AGS cells treated with varying

concentrations of GNP-CK-CopA3 demonstrated the anticancer properties of these nanoparticles. Penetration of GNP-CK-CopA3 into AGS cells was visualized using an enhanced dark field microscope. Apoptosis induction was initially confirmed by treating AGS cells with GNP-CK-CopA3, as evidenced by staining with dyes such as Hoechst and PI. Additionally, mitochondrial disruption and cellular localization induced by GNP-CK-CopA3 were validated through Mito-tracker staining and transmission electron microscopy images. Annexin V-FITC/PI staining was used to distinguish early and late-stage apoptosis or necrosis based on fluorescence patterns. The gene expression of apoptotic markers indicated the initiation of cellular apoptosis. Further, proteomic analysis suggested that the treatment of GNP-CK-CopA3 to AGS cells led to the suppression of 439 proteins and the stimulation of 832 proteins. Among these, ferroptosis emerged as a significant interconnected pathway where glutathione peroxidase 4 (GPX4) and glutathione synthetase (GSS) were significant interacting proteins. Molecular docking and dynamic simulation studies confirmed the binding affinity and stability between CopA3 and CK with GSS and GPX4 proteins, suggesting the role of GNP-CK-CopA3 in ferroptosis induction. Overall, our study showed GNP-CK-CopA3 could play a dual role by inducing apoptosis and ferroptosis to induce AGS cell death.
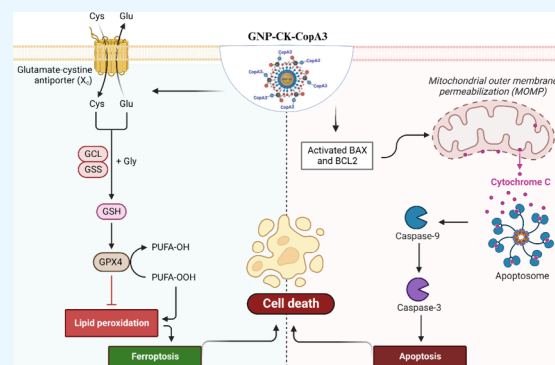
INTRODUCTION

The World Health Organization (WHO) indicated that cancer became the second leading global cause of death by 2022.[1] Despite progress in anticancer drugs like 5-fluorouracil, doxorubicin, and methotrexate, their efficacy is hindered by side effects.[2] Gastric cancer (GC), ranking fourth in cancer-related mortality, poses challenges due to asymptomatic early stages, leading to delayed diagnoses and consequently poor survival rates. With a striking 50% recurrence rate among GC patients, there is an urgent need to identify diagnostic and prognostic biomarkers to guide the development of innovative therapeutic targets.[3] The escalating global impact of cancer has underscored an urgent need for advancements in research and treatment. Therefore, using natural derived nanoparticles that target cell death pathways by imposing minimal side effects is crucial and timely for the treatment of deadly disease like cancer.

The cell death mechanism is a phenomenon the body undergoes to maintain homeostasis and prevent diseases. Apoptosis, a well-characterized process of programmed cell death, manifests distinct cellular features such as cell contraction, chromatin condensation, membrane bleb formation, and DNA fragmentation.[4] While ferroptosis emerged as a novel form of programmed cell death in 2012, as elucidated by Stockwell, it is primarily fueled by iron-driven lipid peroxidation.
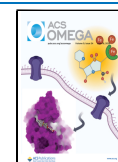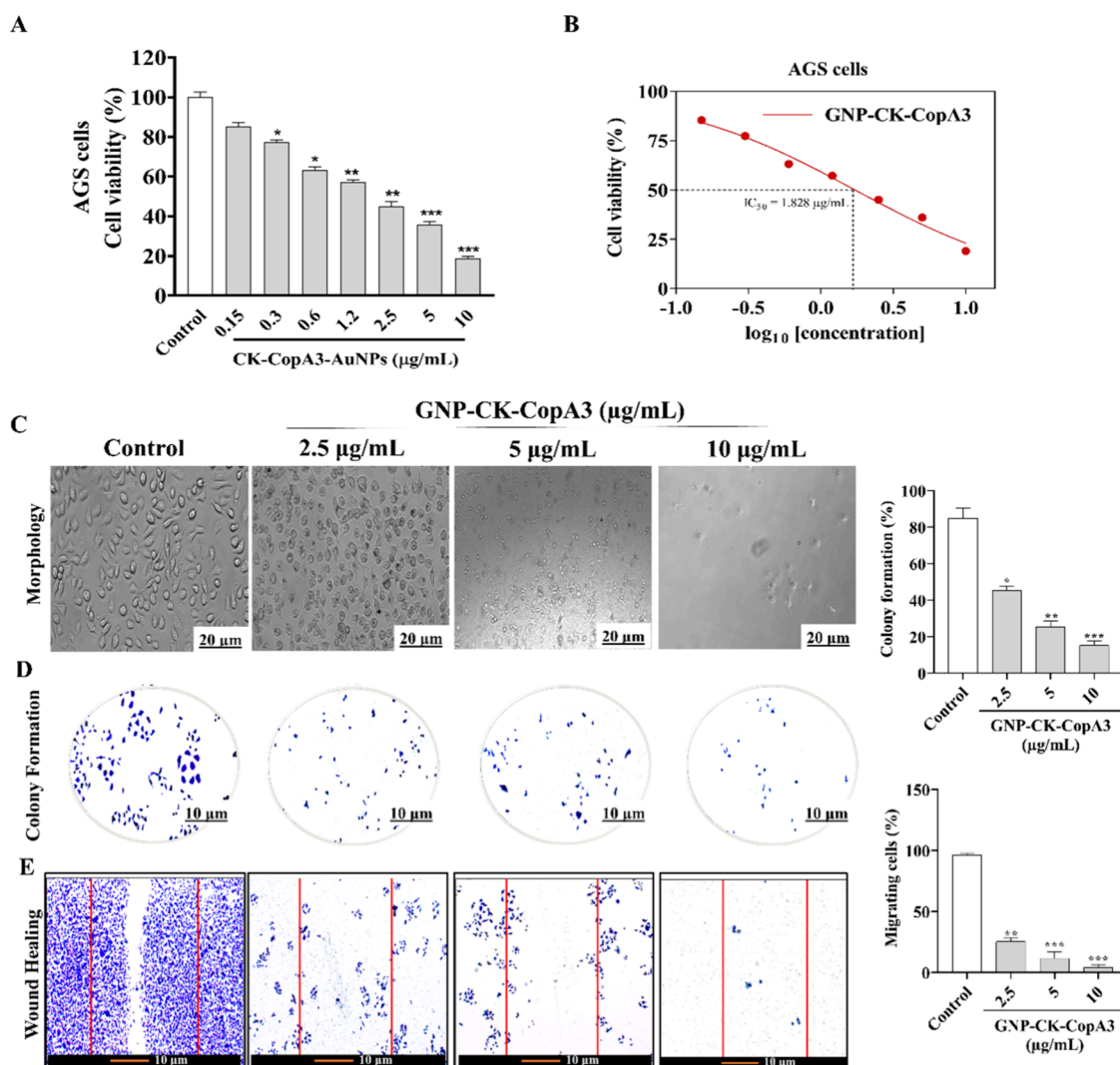
Figure 1. Assessment of cytotoxicity effect on AGS cells. (A-B) The assessment of cell viability postexposure to cytotoxic agents. Quantitative data demonstrates the percentage of viable cells compared to controls, indicating the impact of the treatment on cellular survival. (C) Exhibits changes in cellular morphology induced by the cytotoxic effect. Visual representation elucidates alterations in cell shape, size, and structural integrity, highlighting the impact on cellular architecture. (D) Presents results from the colony formation assay following cytotoxic treatment. This assay assesses cellular proliferative potential, revealing the impact on clonogenicity and the ability to form colonies. (E) Depicts outcomes of the wound healing assay postcytotoxic exposure. It quantifies cell migration ability by measuring the closure of a gap or wound, indicating the influence of cytotoxicity on cellular motility. All images are captured at a magnification of 100× and are accompanied by a scale bar indicating 10 or 20 μm. Each bar represents the mean $\pm$ SEM of duplicate samples from three independent experiments. Statistical significance is denoted as $*p < 0.05$, $**p < 0.01$, and $***p < 0.001$ compared to the untreated control.

Glutathione peroxidase 4 (GPX4), the protein central to this process, predominantly facilitates the transformation of potentially harmful lipid hydroperoxides (L-OOH) into benign lipid alcohols (L-OH).[5] Both ferroptosis and apoptosis can be distinguished by cell morphological characteristics, biochemical features, and other features. Nevertheless, contemporary findings suggest that ferroptosis and apoptosis may synergistically interact or be interchangeably employed to orchestrate cellular demise, contingent upon the cellular milieu and external stimuli.[6] Identifying the potential target that inactivates GPX by depletion of glutathione (GSH) can lead to lipid peroxidation, and activation of programmed cell death is essential.

Gold nanoparticles (GNP) exhibit distinctive optical and physicochemical properties, garnering significant research attention for diverse therapeutic and medical diagnostic applications.[7,8] These GNP have proven successful in enhancing the efficacy and specificity of diagnosis and therapy, minimizing side effects in the process.[9] Their potential for improving the effectiveness of various targeted cancer therapies is well-documented.[9] Researchers have increasingly explored the biological synthesis of GNP due to its simplicity, biocompatibility, and the distinctive physicochemical properties of gold.[9,10] Microorganism synthesis of GNP offers a sustainable and eco-friendly approach, reducing metal ions without producing toxic byproducts. Studies have highlighted the use of *Lactobacillus* strains for extracellular or intracellular biosynthesis of GNP.[11] Despite extensive research into the fundamental anticancer mechanisms of GNP, a precise understanding remains uncertain. Numerous postulated mechanisms include apoptosis and ferroptosis.[12] The integration of gold nanoparticles, nanotechnology, and bacterial synthesis presents a multifaceted approach to addressing the urgent challenges in cancer research and treatment, showcasing the potential for innovative and sustainable solutions. The study aimed to investigate the
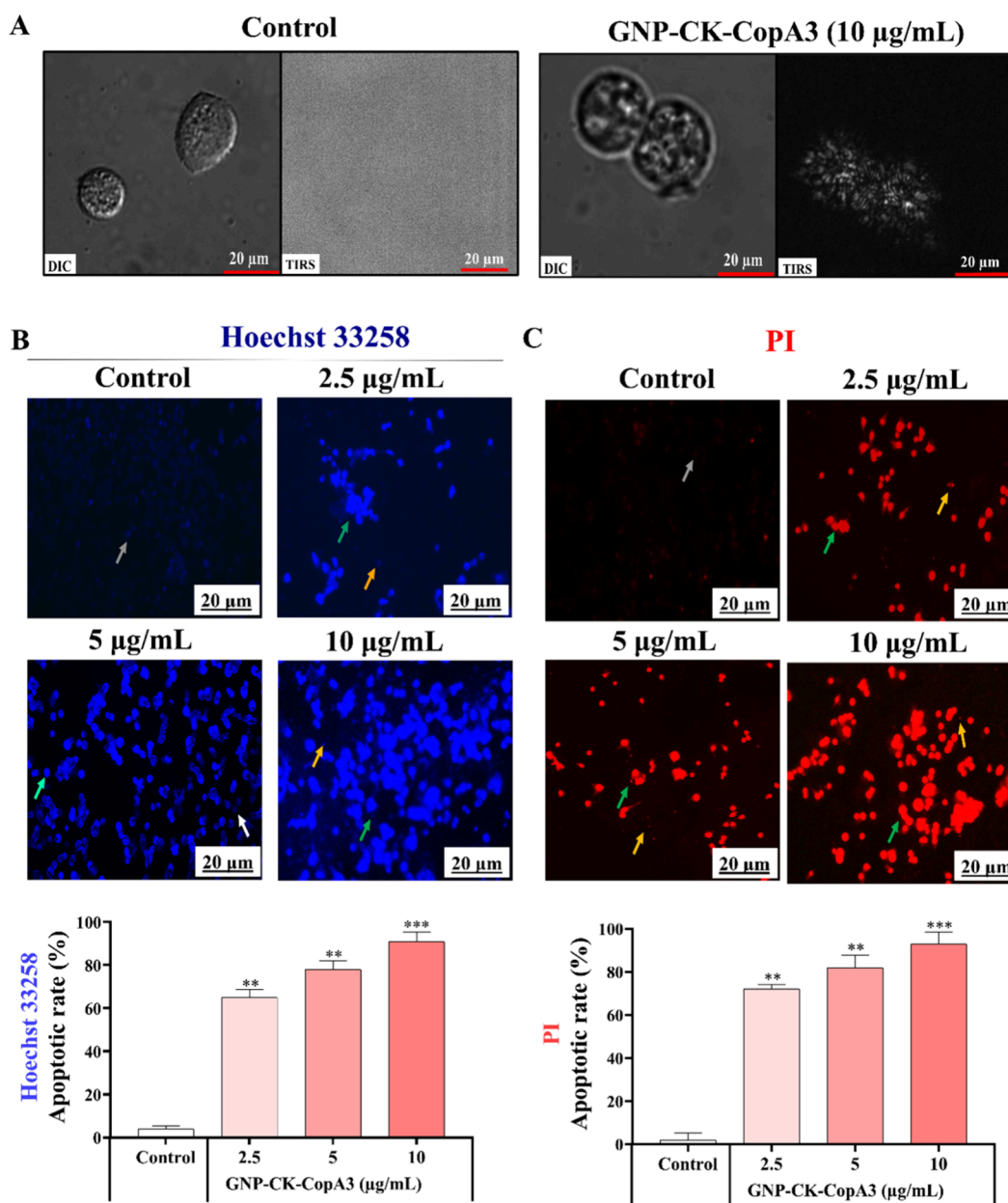
Figure 2. Assessment of cellular uptake and induction of apoptosis by GNP-CK-CopA3 in AGS cells. (A) Illustrates the visualization of GNP-CK-CopA3 uptake within AGS cells using enhanced dark-field (EDF) microscopy. (B) Exhibits the detection of apoptosis induced by GNP-CK-CopA3 through Hoechst 33258 staining. This staining method allows for the visualization of nuclear morphological changes characteristic of apoptotic cells under fluorescence microscopy. (C) Presents the detection of apoptosis induced by GNP-CK-CopA3 through propidium iodide (PI) staining. This staining method enables the identification of cells with compromised membranes, another hallmark of apoptosis, under fluorescence microscopy. All images are captured at a magnification of 100× and are accompanied by a scale bar indicating 20 μm. The abbreviations used in the figure legend are as follows: EDF (enhanced dark-field), DIC (differential interference contrast), TIRS (thermal infrared sensor), and PI (propidium iodide). Each bar represents the mean ± SEM of duplicate samples from three independent experiments. Statistical significance is denoted as *$p < 0.05$, **$p < 0.01$, and ***$p < 0.001$ compared to the untreated control.

anticancer effects of GNP-CK-CopA3 and explore their mechanisms in AGS cells, specifically focusing on their role in apoptosis and ferroptosis activation. This exploration of complex molecular pathways enhances our comprehension of GNP-CK-CopA3 therapeutic effects on AGS, offering valuable insights for potential therapeutic applications in cancer treatment.

■ RESULTS

Cytotoxicity Effect of GNP-CK-CopA3 in AGS Cells. The effect of GNP-CK-CopA3 in HFE-145, KATTO III and AGS cells was assessed using a MTT assay. Initially, the cytotoxic effect of GNP-CK-CopA3 was validated on HFE-145 at concentrations ranging from 0.15 to 10 μg/mL (Figure S1A). The dose-dependent inhibitory effect showed no cytotoxicity, indicating the suitability of these concentrations for further investigations. Subsequently, the impact of GNP-CK-CopA3 on two gastric cancer cell lines, KATTO III and AGS, was examined

(Figure S1B and 1A). Both cell lines exhibited sensitivity to GNP-CK-CopA3, with AGS cells resulting in a higher inhibitory response compared to KATTO III cells. The GNP-CK-CopA3 exhibited cytotoxic effects in AGS cells, as indicated by an IC$_{50}$ value of 1.828 μg/mL. The observed toxicity levels varied with concentrations of 2.5, 5, and 10 μg/mL, resulting in approximate inhibitions of 45%, 35%, and 20%, respectively (Figure 1B). To further substantiate the cytotoxicity of GNP-CK-CopA3, cell morphology, colony formation, and wound healing assays were performed using AGS cells. In the colony formation assay, untreated AGS cells exhibited rapid division and a distinct morphology. However, GNP-CK-CopA3 caused a dose-dependent reduction in cell density, increase in floating cells, and formation of apoptotic bodies (Figure 1C). The untreated control cells produced definite colonies with distinct structures (Figure 1D). In contrast, at a low concentration (2.5 μg/mL), GNP-CK-CopA3 significantly inhibited the colony formation potential, resulting in significant inhibition of AGS cell colonies. The impact of GNP-CK-CopA3 on AGS cell migration was evaluated through a wound healing migration assay. After a 24 h incubation period, notable suppression of cell migration was observed across different concentrations of GNP-CK-CopA3 (2.5, 5, and 10 μg/mL) in comparison to the untreated control group (Figure 1E). Therefore, these results suggest that GNP-CK-CopA3 exhibited potent cytotoxicity on AGS cells by inhibiting cell viability and migration in a dose-dependent manner.

Cellular Uptake and Apoptotic Staining in GNP-CK-CopA3-Treated AGS Cells. To assess the penetration and internalization of GNP-CK-CopA3 into AGS cells, cellular uptake was assessed using enhanced dark field (EDF) microscopy. Following a 3 h incubation, the presence of aggregated bright white spots in Figure 2A indicates that GNP-CK-CopA3 were likely internalized by AGS cells.

Apoptotic cells were assessed through fluorescence staining using Hoechst 33258 and PI dyes (Figure 2B-C). As described in Figure 2B, the untreated control AGS cells exhibited no fluorescence within the stained nuclei, indicating the absence of apoptosis. In contrast, AGS cells treated with GNP-CK-CopA3 (2.5, 5, and 10 μg/mL) demonstrated significant morphological apoptotic changes, including cell rounding and enhanced fluorescence (Figure 2B). PI fluorescence was observed only in damaged, necrotic, and dead cells, whereas no PI fluorescence was detected in the untreated cells. However, PI-stained cells treated with GNP-CK-CopA3 (2.5, 5, and 10 μg/mL) exhibited a significant number of dead cells in the form of colonies (Figure 2C). These results distinctly indicated that GNP-CK-CopA3 induced apoptosis.

Mitochondrial Alterations Induced by GNP-CK-CopA3 in AGS Cells. Mito-Tracker green fluorescent dye was used to assess mitochondrial alterations in AGS cells (Figure 3). In the control group, AGS cells exhibited an unaltered mitochondrial morphology within the cytoplasm. However, following treatment with GNP-CK-CopA3, AGS cells exhibited damage to both inner and outer mitochondrial membranes. This resulted in mitochondrial visualization as a mass of dye and distinct foci, signifying GNP-CK-CopA3-induced damage to AGS cell mitochondria. Significant morphological alterations in the mitochondria were evident between the control group and the cells treated with GNP-CK-CopA3. These differences in observations suggested substantial mitochondrial damage in the GNP-CK-CopA3-treated cells compared to the control.
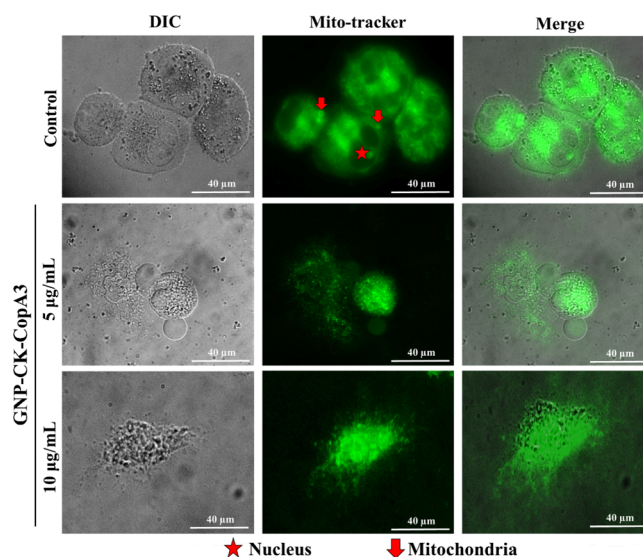

Figure 3. Mito-Tracker staining analysis of GNP-CK-CopA3-treated AGS cells. The figure demonstrates the Mito-Tracker staining analysis conducted on AGS cells treated with GNP-CK-CopA3, observed using an enhanced dark-field (EDF) microscope. The specific visualization of mitochondrial staining using Mito-Tracker in AGS cells treated with GNP-CK-CopA3. All cellular images were captured at an exceptionally high magnification of 1000×, ensuring intricate details are observable, and are accompanied by a scale bar of 40 μm.

Localization of GNP-CK-CopA3. Transmission electron microscopy (TEM) analysis was conducted to ascertain the intracellular distribution and impacts of GNP-CK-CopA3 within AGS cells (Figure 4A). In the TEM images, the untreated control cells exhibited usual cytoplasmic organelles, intact nuclei, and sporadic membranous vacuole structures reminiscent of autophagosomes. However, following a 3 h GNP-CK-CopA3 (5 and 10 μg/mL) treatment, the localization of CopA3-GNP in AGS cells was observed, primarily aggregating within membrane-bound organelles. In addition, pathological changes were observed, such as an increase in autophagic vacuoles, swollen mitochondria and lysosomes, and severely damaged organelles, characterized by double-membrane autophagosomes in both the cytoplasm and nucleus.

Initiation of Apoptosis in AGS Cells by GNP-CK-CopA3. The confirmation of GNP-CK-CopA3 impact on AGS cell apoptosis was established through Annexin V-FITC/PI double staining (Figure 4B). Annexin V detects externalized phosphatidylserine in early apoptotic cells, whereas PI stains the nuclei of necrotic and late apoptotic cells. In untreated cells, the majority of cells (99.3 $\pm$ 0.62%) were viable, with a small percentage exhibiting early or late apoptosis or necrosis. However, GNP-CK-CopA3-treated cells (5 and 10 μg/mL) exhibited a significant increase in early apoptotic cells (62.1 $\pm$ 0.32 and 65.3 $\pm$ 0.45%) and late apoptotic cells (9.4 $\pm$ 0.72 and 23.2 $\pm$ 0.18%), respectively.

For the evaluation of GNP-CK-CopA3-induced apoptosis in AGS cells, an analysis of apoptosis-related gene expression was conducted through qRT-PCR (Figure 4C). The Bcl-2 family of proteins (Bcl-2-associated X protein (Bax) and B-cell lymphoma 2 (Bcl-2)) are significant in apoptosis regulation. Following a 24 h treatment, GNP-CK-CopA3 exhibited a dose-dependent downregulation of the antiapoptotic Bcl-2 gene with an upregulation of the pro-apoptotic Bax gene, resulting in a 6-fold increase in the Bax/Bcl-2 ratio. This suggests that an
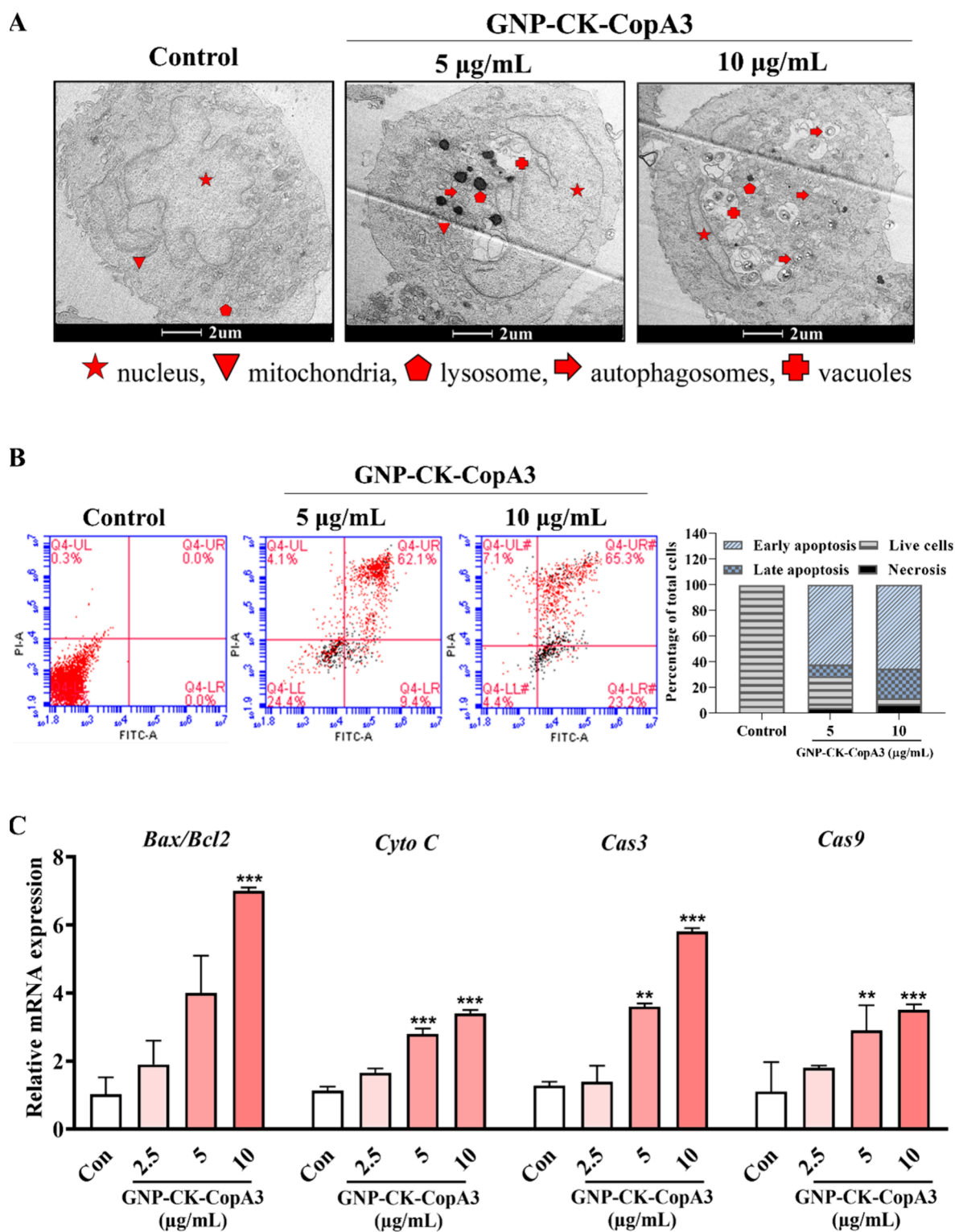
Figure 4. Induction of apoptosis in AGS cells by GNP-CK-CopA3. (A) Exhibits the localization and intracellular distribution of GNP-CK-CopA3 within AGS cells as visualized through transmission electron microscopy (TEM). This high-resolution imaging technique enables precise visualization of nanoparticle localization within cellular compartments. (B) Demonstrates the assessment of apoptosis induction in AGS cells treated with GNP-CK-CopA3 via Annexin V-FITC/PI double staining utilizing flow cytometry. Dot plot diagrams depict distinct cell populations: viable (Annexin V−/PI−), early apoptotic (Annexin V+/PI−), late apoptotic (Annexin V+/PI+), and necrotic cells (Annexin V−/PI+). (C) Presents the quantitative real-time polymerase chain reaction (qRT-PCR) analysis of mRNA expression levels of apoptosis-associated genes, including Bax/Bcl-2, cytochrome c, caspase-9, and caspase-3. β-actin is used as an internal control. Each bar represents the mean ± SEM of duplicate samples from three independent experiments. Statistical significance is denoted as $*p < 0.05$, $**p < 0.01$, and $***p < 0.001$ compared to the untreated control. The abbreviations used in the figure legend are as follows: TEM (transmission electron microscopy), FITC (fluorescein isothiocyanate), PI (propidium iodide), SEM (scanning electron microscopy).
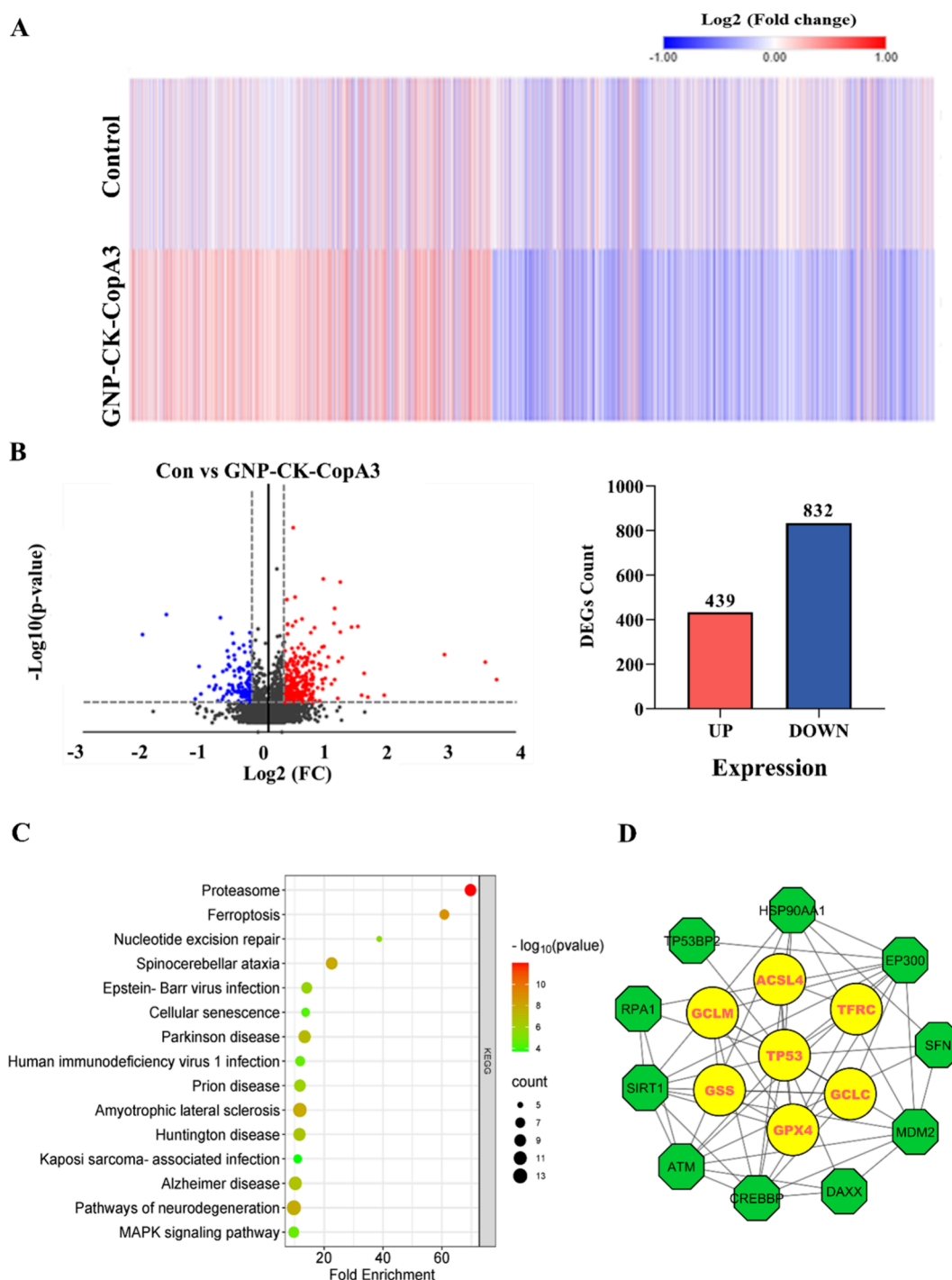
Figure 5. Identification of differentially expressed proteins (DEPs) upon treatment with GNP-CK-CopA3 in AGS cells. (A) Heatmap representation illustrating the expression patterns of total proteins identified in AGS cells treated with GNP-CK-CopA3. The heatmap visualizes the relative expression levels of proteins, depicting their upregulation or downregulation compared to control conditions. (B) Volcano plot exhibiting the distribution of differentially expressed proteins (DEPs). This plot illustrates the fold change in protein expression (x-axis) against statistical significance (y-axis). Total upregulated and downregulated proteins are highlighted, providing a graphical depiction of the protein expression alterations induced by GNP-CK-CopA3 treatment. (C) Kyoto Encyclopedia of Genes and Genomes (KEGG) pathways associated with the identified DEPs upon treatment with GNP-CK-CopA3. This analysis elucidates the biological pathways influenced by the altered protein expression, offering insights into potential molecular mechanisms affected by the treatment. (D) Exhibits the construction of a protein−protein interaction (PPI) network using STRING through Cystoscope software. This network analysis provides a visual representation of the interactions among proteins, allowing the identification of key nodes or clusters within the cellular system affected by GNP-CK-CopA3.

increased Bax/Bcl-2 ratio was associated with GNP-CK-CopA3-induced apoptosis. Additionally, Cytochrome C (CytoC), Caspase 9 (Cas9), and Caspase 3 (Cas3) levels were upregulated in GNP-CK-CopA3-treated AGS cells in a dose-dependent manner. In summary, these findings indicate that GNP-CK-CopA3 induce apoptosis in AGS cells through a mitochondria-mediated intrinsic pathway.

Proteomic Profiling Reveals Differentially Expressed Proteins and Pathways in GNP-CK-CopA3-Treated AGS Cells. In this study, we assessed the protein regulation of GNP-CK-CopA3-treated AGS cells through proteomic analysis. Proteomic analysis was used to identify differentially expressed proteins in AGS cells following treatment with the control and GNP-CK-CopA3. In total, 1,266 differentially expressed proteins were identified in GNP-CK-CopA3 compared with the control (Figure 5A). In the volcano plot and bar chart, 439 proteins were up-regulated and 832 proteins were down-regulated (Figure 5B). Protein pathways were identified using the Kyoto Encyclopedia of Genes and Genomes (KEGG) pathway. As shown in Figure 5C and Table S2, the majority of pathways were related to brain diseases (Parkinson's disease, Alzheimer's disease, neurodegeneration, prion diseases, Huntington's disease, spinocerebellar ataxia, and amyotrophic lateral sclerosis) and viral diseases (Epstein−Barr, Human immunodeficiency virus 1, and Kaposi sarcoma), whereas ferroptosis exhibited a high enrichment value, significant p-value, and connected proteins (transferrin receptor, TFRC; glutamate-cysteine ligase catalytic subunit, GCLC; GPX4; GSS; glutamate-cysteine ligase modifier subunit, GCLM; acyl-coa synthetase long chain family member 4, ACSL4). Therefore, we analyzed the protein−protein interaction (PPI) of ferroptosis pathway-related proteins. In this study, we demonstrated that GPX4 is highly interacting with other proteins (Figure 5D). Our results indicate the significance of ferroptosis pathway for these proteins. Furthermore, these proteins were chosen for molecular docking and dynamic simulations.

Molecular Docking. A molecular docking assessment study demonstrated the binding efficacy of CopA3 and CK structures with their respective receptors. Binding affinity was used to identify the docked complexes. In Figure 6, the binding affinities
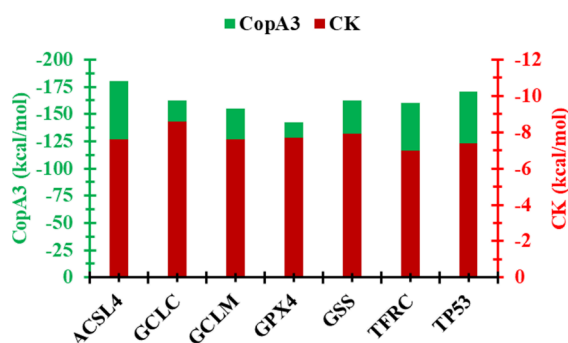

Figure 6. Docking scores of CopA3 peptide and CK compound with target proteins. The bar graph illustrates the docking scores of CopA3 and CK with designated target proteins, showcasing their respective affinity or binding scores. This graph offers insights into the strength of interaction and potential binding affinities of CopA3 and CK toward individual target proteins. These scores serve as crucial indicators, providing valuable information about the plausibility and strength of molecular interactions between the compounds and their specific protein targets.

of CK with GCLC, GSS, GPX4, ACSL4, GCLM, TP53, and TFRC are −8.6, −7.9, −7.7, −7.6, −7.6, −7.4, and −7.0 kcal/mol, respectively, whereas those of CopA3 are −162.22, −162.81, −142.79, −180.49, −155.28, −170.97, and −159.93 kcal/mol. These complexes demonstrated good binding affinities and strong interactions (Figure S2−S3).

Stability of Targeted Proteins with CK and CopA3. To assess the stability of protein structures over the course of simulation time (200 ns), the root-mean-square deviation (RMSD) values of Cα (α carbon) for the targeted proteins ACSL4 (blue), TP53 (orange), GSS (gray), GCLC (gold), TFRC (dark blue), GPX4 (green), and GCLM (blue-gray) were calculated (Figure 7A-B). The GSS protein complexes achieved stability with CopA3 (after 13 ns) and CK (after 30 ns), respectively. During the simulation time (200 ns), average RMSD values (1.887 Å, 2.028 Å) and fluctuation rates (1.372 Å, 1.419 Å) with CopA3 and CK were determined. In this study, GSS exhibited a significant RMSD value with CopA3 and CK, implying a stable complex system. The GPX4-CopA3 complex exhibited stability after 102 ns, with average values of fluctuation (1.711 Å) and RMSD (1.977 Å). Consequently, the GPX4-CK complex exhibited stability after 95 ns, with average values of fluctuation (1.636 Å) and RMSD (1.664 Å). In the protein−ligand network, GPX4 exhibited a stable RMSD value, with the second-lowest difference in RMSD and the second-most stable complex. The GCLM-CopA3 complex exhibited stability between 50 and 120 and 150−200 ns, with average values of fluctuation (1.779 Å) and RMSD (2.251 Å). The GCLM-CK complex exhibited stability after 124 ns, with average values of fluctuation (2.183 Å) and RMSD (2.632 Å). In the protein−ligand network, GCLM exhibited a stable RMSD value, with the third smallest difference in RMSD, and the third-most stable complex. TP53 and GCLC exhibited higher stability than ACSL4 and TFRC, with RMSD values and fluctuation rates consistently <3 Å. This indicated their stability as the fourth and fifth ranked protein−ligand complexes. During the complete simulation time, ACSL4 and TFRC exhibited average RMSD values for CopA3 (3.699 and 6.920 Å) and CK (3.234 and 4.017 Å), respectively. This indicated their instability due to elevated RMSD values and fluctuation rates (Figure 7A-B).

The root-mean-square fluctuation (RMSF) value shows that the stability and fluctuation levels of amino acid residues within the complex system are determined by amino acid residues. The highest fluctuation and average fluctuation values of amino acids for the GSS-CK complex were 3.443 and 1.013 Å, and the GSS-CopA3 complex were 4.636 and 0.976 Å, respectively. The CK with GPX4, GCLM, GCLC, and TP53 complexes displayed the largest fluctuations in amino acid values of 3.491, 7.012, 12.991, 5.352, and 4.636 Å, respectively (Figure 7C-D). The complexes of CK with the amino acids GPX4, GCLM, GCLC, and TP53 exhibited average RMSF values of 0.885, 1.394, 1.196, and 1.181 Å, respectively. The complex of CopA3 with the amino acids GPX4, GCLM, GCLC, and TP53 exhibited average RMSF values of 0.911, 1.097, 0.939, and 1.477 Å, respectively. GSS with CopA3 and CK exhibited the highest stability during the RMSF study (Figure 7C-D).

The number of hydrogen bonds within a protein−ligand complex has a significant impact on binding and adsorption. Therefore, the minimum and maximum number of hydrogen bonds for the GSS-CopA3 complex were 1 and 6, and those for the GSS-CK complex were 1 and 2, respectively (Figure 7E-F). Additionally, we analyzed the ligand RMSD, solvent-accessible surface area (SASA), and *radius of gyration (Rg)* for all proteins and protein-drug complexes. SASA and Rg analyses of GSS, GPX4, and GCLM proteins revealed that CopA3 and CK exhibited significant stability and were the first-, second-, and third-most suitable targets, respectively (Figure S4). Protein−ligand contact analysis revealed significant interactions between GSS and GPX4 (Figure S5−S6). Dynamic simulation results
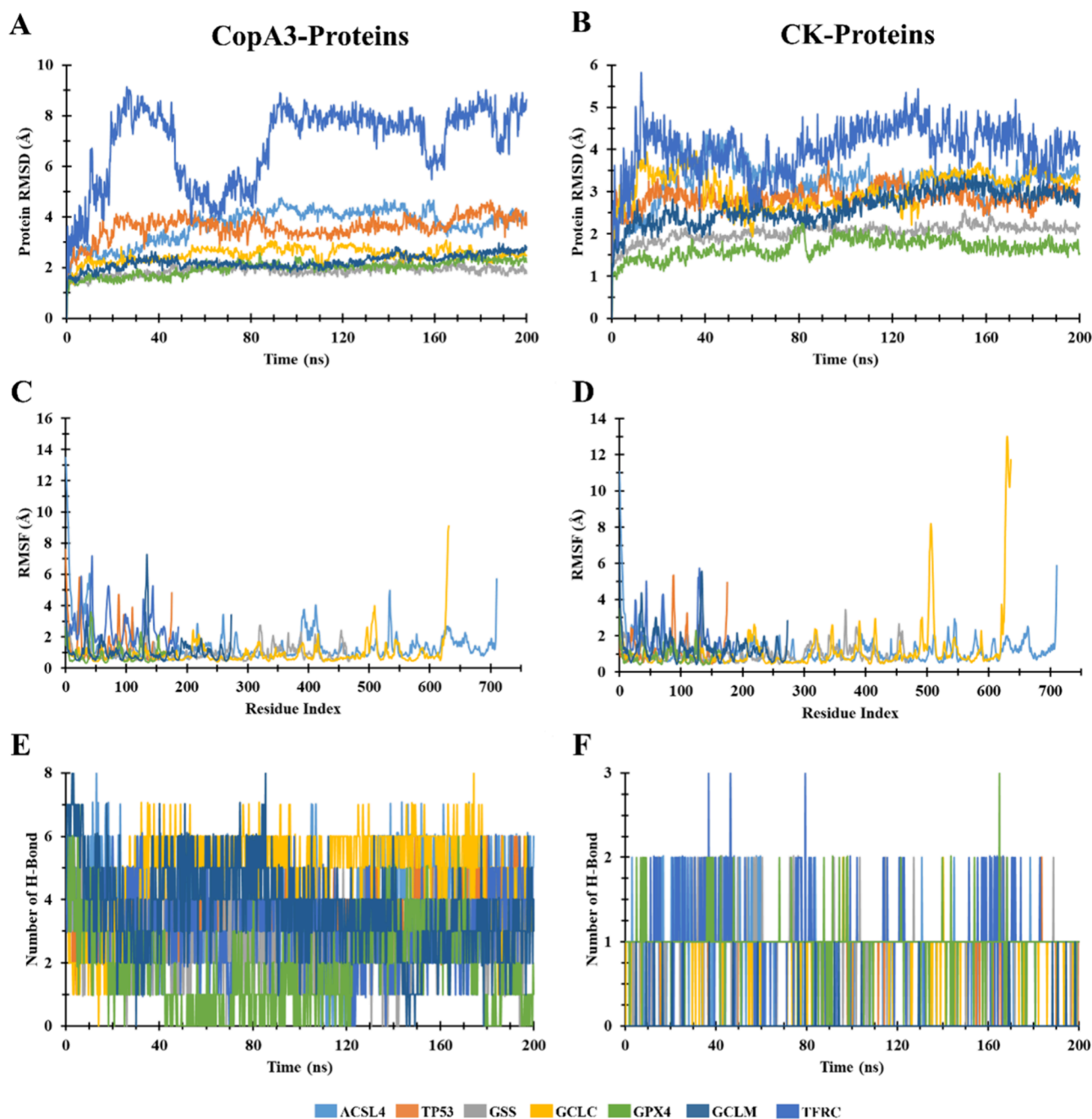
Figure 7. RMSD, RMSF, and hydrogen bonds of targeted proteins with CK and CopA3. (A-B) Illustrate the RMSD profiles of CopA3 and CK interacting with designated proteins over the course of molecular dynamic simulations. These graphs demonstrate the stability and deviation patterns of CopA3 and CK protein complexes throughout the simulation period. (C-D) Depict the root mean square fluctuation (RMSF) values of CopA3 and CK bound to specific proteins. These graphs showcase the residue-wise fluctuations of CopA3 and CK when interacting with individual proteins, providing insights into the dynamic behavior of the complex. (E-F) Represent the count of hydrogen bonds formed between CopA3 or CK and the specified proteins during the molecular dynamic simulation. The color-coded bars indicate the number of hydrogen bonds formed over time, highlighting the varying interaction strengths between CopA3 or CK and different proteins. The color-coded representation distinguishes various proteins: ACSL4 (blue), TP53 (orange), GSS (gray), GCLC (gold), TFRC (dark blue), GPX4 (green), and GCLM (blue-gray), offering a clear comparison of the interactions with CopA3 and CK across the specified proteins.

indicated that the GSS complex with both CopA3 and CK exhibited remarkable stability following the binding of drug molecules.

Visualization of GSS Protein with CopA3 and CK. Studies on protein−ligand interactions are essential for understanding the mechanisms governing biological regulation and serve as a theoretical framework for the development of novel drugs. The interaction of GSS with CopA3 established 19

bonds at various amino acid sites, such as Q96, D97, N271, P272, R273, P365, R367, G371, N372, N373, L374, E378, Q381, A382, Q385, L386, E391, S394, and Y395, respectively (Figure 8A). In addition, GSS and CK formed 13 bonds, such as Q81, G114, I115, A116, Q117, T118, F120, D251, R252, H290, R434, E436, and K437, respectively (Figure 8B). Our study indicates that GSS is a potential target for human gastric cancer, with CK and CopA3 as potential target compounds.
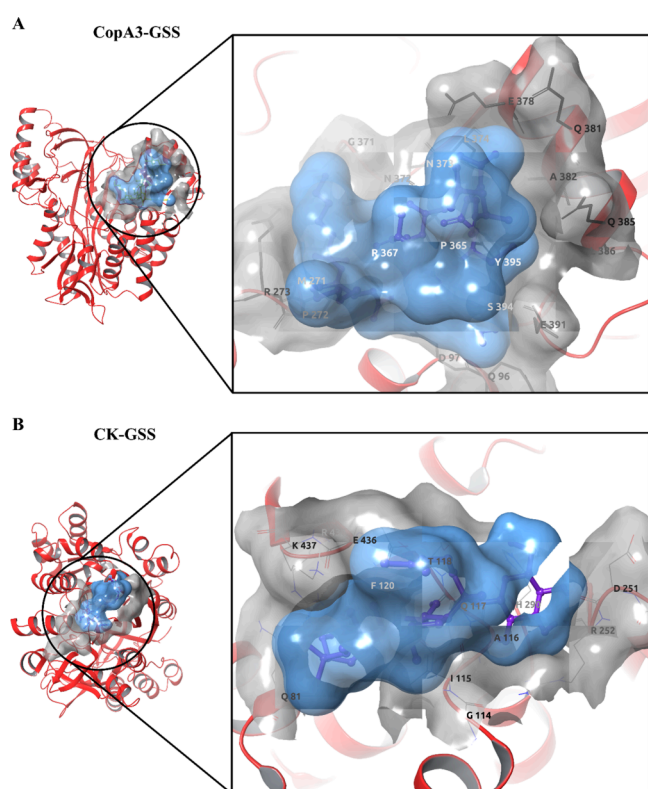
Figure 8. Visualization of the GSS protein interactions with CopA3 and CK. Panel (A) provides a visual depiction of the molecular interactions between the GSS protein and CopA3 compound. This visualization offers insights into (B) the molecular interactions between the GSS protein and the CK compound. This visual representation delineates the structural conformation and putative binding interactions of CK within the GSS protein binding site or active region. The structural arrangement and potential binding modes of CopA3 within the binding site or interface of the GSS protein. These molecular visualizations facilitate a detailed understanding of the molecular docking and potential mechanisms underlying the interactions between the compounds and the GSS protein.

■ DISCUSSION

GNP are utilized in a spectrum of medicinal applications, encompassing targeted delivery and precise release of chemical agents, such as anticancer drugs, peptides, and antibodies.[13] Numerous studies have highlighted the potential of GNP for drug delivery in cancer therapies, such as 5-fluorouracil, doxorubicin, and curcumin.[14−16] Also, previous studies discovered CK and CopA3 exhibited anticancer and anti-inflammatory properties.[17,18] However, the relevant effects of GNP-conjugated CK and CopA3 in anticancer studies are uncertain. Our data substantiates the hypothesis that a distinctive proteomic network, molecular docking, and dynamic simulation governs GNP-CK-CopA3-induced cancer cell death. However, due to their low bioavailability and nonspecific targets, synthesizing GNP conjugated CK and CopA3 can improve all the disadvantages associated with natural compounds with improved anticancer effects. Our data support the hypothesis that a unique proteomic network, molecular docking, and dynamic simulation governs GNP-CK-CopA3 induced cancer cell death.

GNP have the potential to enhance the stability of CK over an extended duration. Conjugating the CopA3 peptide to the surface of GNP could further promote both stability and the

internalization of nanoparticles.[18] In this study, the uptake and localization of GNP-CK-CopA3 within AGS cells were investigated using both EDF and TEM systems. Previous findings suggest that the effectiveness of anticancer treatments is notably influenced by the cellular internalization of drugs. The mechanisms accountable for the cellular uptake of drug-loaded nanoparticles are predominantly associated with macropinocytosis, clathrin-mediated endocytosis, and caveolae-dependent endocytosis.[19] Indeed, doxorubicin-tethered responsive GNP have been demonstrated to enhance intracellular drug delivery, thereby addressing multidrug resistance in cancer cells.[20] This phenomenon is attributed to the highly effective cellular uptake via endocytosis, followed by an acid-responsive release within cells.[21] Additionally, the outcomes indicated that GNP-CK-CopA3 lead to an elevation in damaged nuclei, vacuole formation, and the presence of double-membrane autophagosomes within the cytoplasm. Previous reports have noted that changes in cellular morphology, including alterations in the nucleus, vacuole formation, and the appearance of autophagosomes in the cytoplasm, signify cellular changes indicative of a dying cell.[22]

A comprehensive investigation of the impact of GNP-CK-CopA3 on AGS cells involved a series of experimental analyses. These encompassed proliferation, colony formation, migration assays, Hoechst 33258 staining, PI staining, Annexin V-FITC/PI double staining, Mito-Tracker fluorescence staining, and assessment of apoptosis-related gene expression. GNP-CK-CopA3 demonstrated significant inhibition of cell proliferation, colony formation, and migration activities at concentrations of 2.5, 5, and 10 μg/mL. Apoptotic changes, evidenced by condensed nuclei and the presence of apoptotic bodies, were observed in GNP-CK-CopA3-treated cells compared to control cells with normal nuclei in Hoechst 33258 and PI staining. Moreover, treatment with CK-loaded GNP (DCY51T-AuCKNps) induced apoptotic alterations, characterized by the appearance of apoptotic nuclei in AGS cells and HT29 colon cancer cells.[23] Moreover, it has been reported that CopA3 demonstrates selective pro-apoptotic effects in human gastric and colorectal cancer.[17,24] Hence, the induction of apoptosis by GNP-CK-CopA3 suggests a synergistic effect arising from the combination of ginsenoside CK and peptide CopA3. The apoptotic effects induced by GNP-CK-CopA3 were further validated through Annexin V-FITC/PI double staining analyzed via flow cytometry. This method enabled the detection of various cell populations within AGS cells, including surviving, early apoptotic, late apoptotic, and necrotic cells. GNP-CK-CopA3 administration resulted in an increase of both early apoptotic and late apoptotic cell populations. Similarly, previous studies have reported that ginsenoside CK significantly promoted early and late stages of apoptosis in various human cancer types such as lung carcinoma, leukemia, breast cancer, colorectal cancer, prostate cancer, gastric carcinoma, nasopharyngeal carcinoma, and pulmonary adenocarcinoma.[25]

Additionally, gene expression analysis revealed that GNP-CK-CopA3 significantly upregulated the Bax/Bcl-2 ratio along with increased expression of *Cyto C*, *Cas9*, and *Cas3* genes. Recent studies have demonstrated the development of dual drug-conjugated nanoparticles that induce apoptosis by affecting the mitochondrial outer membrane, resulting in the release of *Cyto C*. These nanoparticles also impact nuclear DNA and the cytoskeletal protein tubulin in HeLa cervical cancer cells.[26] In this study, impairment of the mitochondrial outer membrane in AGS cells was observed through mito-tracker staining, revealing

an accumulation of dye and the presence of distinct foci within the mitochondria. Anticancer peptides are considered promising agents for cancer treatment, as they facilitate intrinsic apoptosis by disrupting the mitochondrial outer membrane. The conjugation of these peptides to GNP notably enhances mitochondrial disruption and pro-apoptotic activity. This enhancement is attributed to the multivalency of peptides provided by GNP on their surface, thereby intensifying their pro-apoptotic effects.[27] Collectively, GNP-CK-CopA3 demonstrated potent anticancer effects by activating the intrinsic-mediated apoptosis pathway.

Additionally, treatment with GNP-CK-CopA3 resulted in 439 up-regulated and 832 down-regulated common differentially expressed proteins when compared to the control group. Through KEGG pathways analysis, we identified ferroptosis pathways proteins including GSS, TFRC, GCLC, GPX4, GCLM, GSS, and ACSL4 upon GNP-CK-CopA3 treatment, suggesting potential therapeutic strategies. Later, we also identified ferroptosis interacting PPI and discovered GPX4 and GSS interacted well with other proteins. Researchers observed that the conversion of GSH to GSS and the aberration in their synthesis leads to the occurrence of ferroptosis. Alternatively, the enzyme GPX4 functions in an inverse manner within this mechanism.[28,29] As expected, these findings provide further evidence suggesting that GNP-CK-CopA3 are involved in the regulation of ferroptosis signaling pathways within AGS cells.

Utilizing molecular docking and dynamic simulations, this study elucidated CK and CopA3 and their associated protein candidates, correlating them with ferroptosis and gastric cancer pathways, thus offering insights into their putative roles in these biological phenomena. The molecular docking procedure was initially utilized to determine the binding affinities of CopA3 and CK with proteins. The first, second, and third binding affinities for the CopA3 peptide, ACSL4, TP53, and GSS proteins were all negative, whereas the GCLC, GSS, and GCLM were the first, second, and third binding affinities for the CK compound. Researcher has identified the high binding affinity showed the stable binding mode(s) of a ligand with a protein at the atomic level.[30] Later, we examined the dynamic simulation of the targeted proteins after docking. The stability of a protein in a combination with ligands was verified using molecular dynamics simulation.[31] The best stability of the compounds is indicated by the RMSD values of complex systems, while RMSF values measure mean fluctuation, which determines how compact the protein−ligand complex.[32] The lowest RMSD and RMSF values were displayed by the GSS, GPX4, and GCLM (average RMSD and RMSF: < 2 Å), excluding others proteins. The GSS and GPX4 protein with CopA3 and CK has been shown to be the most stable due to the study of ligand RMSD, Rg value, SASA values, hydrogen bond interaction, and protein−ligand contact yielding various results.

Numerous published reports have demonstrated that GNP serve as exceptional drug carriers, and therapies utilizing GNP for cancer cells often involve actions related to ferroptosis. For instance, conjugated GNP have been utilized in treating cancer stem cells by inducing cell death through ferroptosis. These therapies aim to enhance iron accumulation and ROS generation while depleting glutathione (GSS) and GPX-4 to induce the process of ferroptosis.[33,34] Through the suppression of GPX4-GSS axis activity, ammonium ferric citrate caused ferroptosis in nonsmall-cell lung carcinoma.[35] Based on the proteomics, docking, and dynamic simulation analysis, ferrop-tosis-related proteins were explored upon GNP-CK-CopA3, CK, and CopA3 treatment to regulate the ferroptosis pathway.

■ CONCLUSION

Our investigation demonstrates the potential anticancer effects of GNP-CK-CopA3 against AGS cells via apoptosis and ferroptosis pathway. GNP-CK-CopA3 exhibited inhibitory effects on cell proliferation and migration while inducing nuclear and mitochondrial damage, primarily through the initiation of mitochondrial-mediated apoptosis. Proteomic and PPI analyses suggested the involvement of GNP-CK-CopA3 in activating the ferroptosis pathway. Molecular docking and dynamic simulation analyses further revealed GSS and GPX4 as potential proteins interacting with CopA3 and CK. Additionally, exploration of the ferroptotic cell death mechanism induced by GNP-CK-CopA3 in AGS cells requires an in-depth analysis of the expression profiles of crucial genes and regulated proteins based on the findings from proteomics. Moreover, our research offers initial data that can be utilized in the creation of new potential anticancer agents, shedding light on their mechanisms. This study serves as a promising foundation for the exploration and development of alternative medications centered around GNP-CK-CopA3. Furthermore, for the extensive industrial application of GNP-CK-CopA3, it is imperative to conduct additional investigations, including *in vivo* studies and clinical trials. These endeavors will delve into the impact of GNP-CK-CopA3 on human health, addressing aspects of safety and anticancer efficacy. Such comprehensive assessments are slated for inclusion in our future research.

■ MATERIALS AND METHODS

Materials. MRS (de Man, Rogosa, and Sharpe) broth and agar were procured from MB Cell (Seoul, Republic of Korea). Fetal bovine serum (FBS) and penicillin-streptomycin were sourced from GenDEPOT (Barker, TX). Gold(III) chloride trihydrate (HAuCl$_4$·3H$_2$O), 3-(4,5-dimethylthiazol-2-yl)-2,5-diphenyltetrazolium bromide (MTT), dimethyl sulfoxide (DMSO), lipopolysaccharide (LPS, *Escherichia coli* 011: B4), and all other chemicals were obtained from Sigma-Aldrich Chemicals (St. Louis, MO, USA). All procedures adhered to relevant guidelines and regulations.

Synthesis and Characterization of GNP-CK-CopA3. The synthesis of ginsenoside CK-loaded gold nanoparticles (GNP-CK) followed our published protocol,[36] involving cultivation of *G. liquefaciens* kh-1 in MRS broth, collection of fresh biomasses, and synthesis of GNPs with HAuCl$_4$·3H$_2$O and CK. After ultrasonication and centrifugation, CK-loaded nanoparticles (GNP-CK) were collected and resuspended in sterile water. To conjugate the peptide CopA3, a carboxylic acid-terminated alkanethiol monolayer was formed on the nano-particle's surface. CopA3 was added to the 1-ethyl-3-(3-dimethylamino-propyl) carbodiimide hydrochloride (EDC) and *N*-hydroxysulfosuccinimide (Sulfo-NHS) activated nano-particles, and the reaction was allowed to proceed before quenching excess hydroxylamine with glycine and Tris. The resulting GNP-CK-CopA3 hybrids were dissolved in sterile water and stored at −20 °C for further study. In a previous study,[36] we detailed a comprehensive procedure for preparing, synthesizing, and characterizing GNP-CK-CopA3. Various instrumental techniques were employed, as reported previously, including ultraviolet−visible (UV−Vis), high-resolution trans-mission electron microscopy (HR-TEM), elemental mapping,

X-ray diffraction (XRD), selected area diffraction (SAED), energy-dispersive X-ray (EDX), dynamic light scattering (DLS), photoluminescence (PL), and Fourier-transform infrared (FTIR).

Cell Culture and GNP-CK-CopA3 Treatment. Human gastric cancer cells (AGS and KATTO III) and gastric epithelial cells (HFE-145) were obtained from the American Type Culture Collection (ATCC; Manassas, VA, USA). All cells were cultured in DMEM with 10% heat-inactivated FBS and 1% PS, maintained at 37 °C in a humidified incubator with 5% CO2 and 95% air. Briefly, the cells were seeded at an initial density of 1×10^4 cells/well in a 96-well plate and allowed to stabilize. After 24 h, the cells were treated with different concentrations of GNP-CK-CopA3, ranging from 0.15 to 10 μg/mL. The seeding plates and specific treatment concentrations are detailed in the following sections for each experiment.

Cytotoxicity Assessment. Cultured cells were treated with varying concentrations of GNP-CK-CopA3 (0.15, 0.3, 0.6, 1.2, 2.5, 5, and 10 μg/mL) for 24 h in 96-well plates. Following treatment, MTT solution (0.5 mg/mL) was added to each well and incubated for 3 h, allowing viable cells to convert it into formazan crystals. Formazan crystals were dissolved using DMSO, followed by agitation for 15 min, and the absorbance at 570 nm was measured using a microplate reader, allowing assessment of cytotoxicity by quantifying cell viability based on the absorbance levels.

Cell Morphology, Colony Formation, and Wound Healing Assay. In cell morphology analysis, AGS cells were initially cultured overnight in a 96-well plate and then exposed to different concentrations of GNP-CK-CopA3 (2.5, 5, and 10 μg/mL) for 24 h. For the colony formation assay, AGS cells were seeded in 6-well plates, treated with varied GNP-CK-CopA3 concentrations for 24 h. Visible colonies were stained with 0.1% crystal violet for 30 min at room temperature. In the wound healing assay, AGS cells were grown in 6-well plates for 24 h, wounded using a pipet tip (200 μL), treated with GNP-CK-CopA3 for 24 h, stained with 0.1% crystal violet, and observed. All the cells were observed using a Leica Microsystem CMS GmbH microscope (Wetzlar, Germany).

Enhanced Dark-Field (EDF) Microscopy Analysis. The AGS cells were initially seeded in cell culture dishes and stabilize for 24 h. After this period, they were exposed to a fresh culture medium supplemented with GNP-CK-CopA3 at a concentration of 10 μg/mL and incubated for 3 h. The culture medium was removed, and the cells were gently washed twice with PBS to remove any excess nanoparticles. Subsequently, the cells were fixed using paraformaldehyde solution (4%) to maintain their structure for visualization of GNP-CK-CopA3 uptake. Images depicting the cellular uptake of the nanoparticles were acquired using an EDF microscopic system (CytoViva Inc., Auburn, AL, USA).

Hoechst 33258, Propidium Iodide and Mito-Tracker Staining. The AGS cells were initially cultured on microscope coverslips within a 6-well plate, allowing them to adhere overnight. After this adherence period, the cells were exposed to various concentrations of GNP-CK-CopA3 (2.5, 5, and 10 μg/mL) for 24 h. Subsequent to the treatment, the cells were rinsed twice with PBS, fixed with 4% paraformaldehyde solution, and stained with 5 μL of Hoechst 33258 and PI solution at 37 °C for 30 min. Apoptotic cells, identifiable by condensed and fragmented nuclei, were observed and visualized using a Leica DMLB fluorescence microscope manufactured by Leica in Wetzlar, Germany.

Mito-Tracker Staining. The AGS cells were placed onto 22 mm coverslips within 6-well plates and exposed to different concentrations of GNP-CK-CopA3 (5 and 10 μg/mL) for a span of 6 h. Following the manufacturer's instructions, these cells were treated with 1 mL of culture medium that included 50 nM Mito-Tracker Green FM, a fluorescent dye designed to target mitochondria with wavelengths of 490/516 nm for excitation/emission. After a 30 min period of incubation, the cells underwent observation and analysis using a Leica DM IRB inverted fluorescence microscope crafted by Leica in Wetzlar, Germany.

Transmission Electron Microscopy (TEM) Analysis. AGS cells were cultured in 6-well plates for 24 h before being exposed to varying concentrations of GNP-CK-CopA3 (5 and 10 μg/mL) for 3 h. Following a standard procedure, cells were washed with PBS thrice and then centrifuged at 8000 rpm, 4 °C for 10 min to collect cell pellets. The pellets underwent fixation with glutaraldehyde (2.5%) for 8 h, followed by postfixation using osmium tetroxide (1%) for 2 h. Subsequent steps included dehydration in an ethanol series (50, 70, 90, and 100%) for 15 min each, embedding in a propylene oxide and Epon resin mixture (2:1 ratio), solidifying at 50 °C for 24 h, and at 60 °C for 48 h. Ultrathin sections (70 nm) were prepared using a Leica EM UC7 ultramicrotome, stained with 3% uranyl acetate and lead citrate, and observed using a JEOL JEM-1010 transmission electron microscope operating at 80 kV.

Annexin V- FITC/PI Double Staining Analysis. The Annexin V-fluorescein isothiocyanate (FITC) Apoptosis Detection Kit from BD Pharmingen in San Diego, CA, USA, was utilized for this assay. AGS cells cultured in 6-well plates underwent incubation with various concentrations of GNP-CK-CopA3 (5 and 10 μg/mL) for a duration of 24 h. The cells were washes with PBS and subsequently centrifuged at 8000 rpm, 4 °C for 10 min. The cells were then suspended in 100 μL of buffer containing 5 μL of Annexin V-FITC and PI stain, followed by a 30 min incubation in darkness at room temperature. Addition of 400 μL of binding buffer facilitated analysis of the samples using a BD AccuriTM C6 Plus Flow Cytometer System located in San Jose, CA, USA.

Quantitative Reverse Transcription-Polymerase Chain Reaction (qRT-PCR) Analysis. AGS cells were grown in 100 mm culture dishes and exposed to varying concentrations of GNP-CK-CopA3 (2.5, 5, and 10 μg/mL). Following 24 h of exposure, total RNA was extracted using the TRIzol reagent kit from Invitrogen in Carlsbad, CA, USA. Complementary DNA (cDNA) was synthesized according to the manufacturer's guidelines using the Superscript First-Strand Synthesis Kit, also from Invitrogen. Quantitative reverse transcription-polymerase chain reaction (qRT-PCR) was carried out using the SYBR Green Sensimix Plus Master Mix from Quantace in Watford, England, with β-actin serving as the reference standard. Table S1 shows the list of primers used in this study.

Identification of Proteins from Proteomics Study. Proteomic analysis was conducted to assess the mechanisms by which GNP-CK-CopA3 influenced specific proteins in AGS cells. Comprehensive protocols for protein preparation, digestion, tandem mass tag (TMT) labeling, high-pH fractionation, liquid chromatography-tandem mass spectrometry (LC-MS/MS) analysis, and data processing are documented in the Supplementary section 1.

Molecular Docking and Dynamic Simulation. Molecular docking was used to determine the binding affinity between the receptors and ligands. The binding affinities of the CopA3

peptide and CK with the targeted proteins analyzed using the HDOCK server and PyRx software, respectively. To assess receptor−ligand stability, a dynamic simulation (200 ns) was performed using the Schrödinger 2023-3 packages. The dynamic simulation quality from the trajectory was analyzed using the Schrödinger SID module. Additional procedures and resources are documented in the Supplementary section 2.

Statistical Analysis. The experiments were conducted in triplicates, and the data are expressed as mean ± standard error of the mean (SEM). Statistical significance was evaluated using Student's t test, with significance levels set at p-values of < 0.05, < 0.01, and <0.001.

■ ASSOCIATED CONTENT

ⓈⒾ Supporting Information

The Supporting Information is available free of charge at https://pubs.acs.org/doi/10.1021/acsomega.4c00554.

> Proteomic study; Protein preparation and digestion; Tandem mass tags (TMT) labeling and high-pH fractionation; Liquid chromatography-tandem mass spectrometry (LC-MS/MS) analysis; Data processing; Downstream analysis; Computational study; Molecular docking; Molecular dynamic simulation; List of primer sequence used in this study; KEGG pathway enrichment values; Cell viability in HFE145 and KATTO III cells; Molecular docking 3D interaction; Molecular docking 2D interaction; Graphs represent the MD simulation result by 200 ns time; Bar graphs presenting targeted proteins-CopA3 interaction; Bar graphs presenting targeted proteins-CopA3 interaction (PDF)

■ AUTHOR INFORMATION

Corresponding Authors

Yeon-Ju Kim − *Graduate School of Biotechnology, and College of Life Science, Kyung Hee University, Yongin-si, Gyeonggi-do 17104, Republic of Korea;* ⓞ orcid.org/0000-0002-3474-066X; Email: yeonjukim@khu.ac.kr

Haribalan Perumalsamy − *Center for Creative Convergence Education, Hanyang University, Seoul 04763, Republic of Korea; Research Institute for Convergence of Basic Science, Hanyang University, Seoul 04763, South Korea;* Email: harijai2004@gmail.com

Authors

Sanjeevram Dhandapani − *Graduate School of Biotechnology, and College of Life Science, Kyung Hee University, Yongin-si, Gyeonggi-do 17104, Republic of Korea*

Abdus Samad − *Graduate School of Biotechnology, and College of Life Science, Kyung Hee University, Yongin-si, Gyeonggi-do 17104, Republic of Korea*

Ying Liu − *Graduate School of Biotechnology, and College of Life Science, Kyung Hee University, Yongin-si, Gyeonggi-do 17104, Republic of Korea*

Rongbo Wang − *Graduate School of Biotechnology, and College of Life Science, Kyung Hee University, Yongin-si, Gyeonggi-do 17104, Republic of Korea*

Sri Renukadevi Balusamy − *Department of Food Science and Biotechnology, Sejong University, Gwangjin-gu, Seoul 05006, Republic of Korea*

Complete contact information is available at:
https://pubs.acs.org/10.1021/acsomega.4c00554

Author Contributions

¶S.D. and A.S. contributed equally. S.D.: Conceptualization, Methodology, Data curation, writing−Original Draft-Review & Editing; A.S.: Formal analysis, writing−Original Draft; Y.L.: Conceptualization, Investigation; R.W.: Data curation, writing−Original Draft-Review & Editing; S.R.B.: Data interpretation and critical manuscript editing; H.P.: Methodology, Data curation, Formal analysis; Y.-J.K.: Project administration, Supervision.

Notes

The authors declare no competing financial interest.

■ ACKNOWLEDGMENTS

■ ABBREVIATIONS

MTT, 3-(4, 5-dimethylthiazol-2-yl)-2,5-diphenyltetrazolium bromide; ACSL4, acyl-CoA synthetase long chain family member 4; FITC, Annexin V-fluorescein isothiocyanate; CK, compound K; CopA3, coprisin; DMSO, dimethyl sulfoxide; DIC, differential interference contrast; EDF, enhanced dark field microscope; GCLC, glutamate-cysteine ligase catalytic subunit; GCLM, glutamate-cysteine ligase modifier subunit; GPX4, glutathione peroxidase 4; GSS, glutathione synthetase; GNP, gold nanoparticles; AGS, human gastric adenocarcinoma; KEGG, Kyoto Encyclopedia of Genes and Genomes; L-OH, lipid alcohols; L-OOH, lipid hydroperoxides; PI, propidium iodide; PPI, protein−protein interaction; Rg, radius of gyration; RMSD, root-mean-square deviation; RMSF, root-mean-square fluctuation; SASA, solvent-accessible surface area; TFRC, transferrin receptor; TIRS, thermal infrared sensor

■ REFERENCES

(1) Siegel, R. L.; Miller, K. D.; Fuchs, H. E.; Jemal, A. Cancer statistics, 2022. *CA Cancer J. Clin* **2022**, *72* (1), 7−33.

(2) Ketabat, F.; Pundir, M.; Mohabatpour, F.; Lobanova, L.; Koutsopoulos, S.; Hadjiiski, L.; Chen, X.; Papagerakis, P.; Papagerakis, S. Controlled Drug Delivery Systems for Oral Cancer Treatment-Current Status and Future Perspectives. *Pharmaceutics* **2019**, *11* (7), 302.

(3) Li, Y.-N.; Xie, B.; Zhang, Y.; He, M.-H.; Xing, Y.; Mu, D.-M.; Wang, H.; Guo, R. Advances and key focus areas in gastric cancer immunotherapy: A comprehensive scientometric and clinical trial review (1999−2023). *World Journal of Gastroenterology* **2023**, *29* (40), 5593−5617.

(4) Ketelut-Carneiro, N.; Fitzgerald, K. A. Apoptosis, Pyroptosis, and Necroptosis-Oh My! The Many Ways a Cell Can Die. *J. Mol. Biol.* **2022**, *434* (4), 167378.

(5) Yang, J.; Hu, S.; Bian, Y.; Yao, J.; Wang, D.; Liu, X.; Guo, Z.; Zhang, S.; Peng, L. Targeting cell death: pyroptosis, ferroptosis, apoptosis and necroptosis in osteoarthritis. *Frontiers in Cell and Developmental Biology* **2022**, *9*, 789948.

(6) Wu, P.; Zhang, X.; Duan, D.; Zhao, L. Organelle-Specific Mechanisms in Crosstalk between Apoptosis and Ferroptosis. *Oxidative Medicine and Cellular Longevity* **2023**, *2023*, 3400147.

(7) Dhandapani, S.; Wang, R.; cheol Hwang, K.; Kim, H.; Kim, Y.-J. Exploring the potential anti-inflammatory effect of biosynthesized gold nanoparticles using Isodon excisus leaf tissue in human keratinocytes. *Arabian Journal of Chemistry* **2023**, *16* (10), 105113.

(8) Kim, S.; Wang, R.; Dhandapani, S.; Kang, K.; Cho, I.-H.; Kim, Y.-J. Novel modified probiotic gold nanoparticles loaded with ginsenoside

CK exerts an anti-inflammation effect via NF-κB/MAPK signaling pathways. *Arabian Journal of Chemistry* **2024**, *17* (4), 105650.

(9) Dhandapani, S.; Xu, X.; Wang, R.; Puja, A. M.; Kim, H.; Perumalsamy, H.; Balusamy, S. R.; Kim, Y. J. Biosynthesis of gold nanoparticles using Nigella sativa and Curtobacterium proimmune K3 and evaluation of their anticancer activity. *Mater. Sci. Eng. C Mater. Biol. Appl.* **2021**, *127*, 112214.

(10) Wang, R.; Moon, S.-K.; Kim, W.-J.; Dhandapani, S.; Kim, H.; Kim, Y.-J. Biologically Synthesized Rosa rugosa-Based Gold Nanoparticles Suppress Skin Inflammatory Responses via MAPK and NF-κB Signaling Pathway in TNF-α/IFN-γ-Induced HaCaT Keratinocytes. *ACS omega* **2022**, *7* (40), 35951−35960.

(11) Markus, J.; Mathiyalagan, R.; Kim, Y. J.; Abbai, R.; Singh, P.; Ahn, S.; Perez, Z. E. J.; Hurh, J.; Yang, D. C. Intracellular synthesis of gold nanoparticles with antioxidant activity by probiotic Lactobacillus kimchicus DCY51(T) isolated from Korean kimchi. *Enzyme Microb Technol.* **2016**, *95*, 85−93.

(12) Dhandapani, S.; Xu, X.; Wang, R.; Puja, A. M.; Kim, H.; Perumalsamy, H.; Balusamy, S. R.; Kim, Y.-J. Biosynthesis of gold nanoparticles using Nigella sativa and Curtobacterium proimmune K3 and evaluation of their anticancer activity. *Materials Science and Engineering: C* **2021**, *127*, 112214.

(13) Oladipo, A. O.; Lebelo, S. L.; Msagati, T. A. M. Nanocarrier design-function relationship: The prodigious role of properties in regulating biocompatibility for drug delivery applications. *Chem. Biol. Interact* **2023**, *377*, 110466.

(14) Gao, Q.; Feng, J.; Liu, W.; Wen, C.; Wu, Y.; Liao, Q.; Zou, L.; Sui, X.; Xie, T.; Zhang, J.; et al. Opportunities and challenges for co-delivery nanomedicines based on combination of phytochemicals with chemotherapeutic drugs in cancer treatment. *Adv. Drug Deliv Rev.* **2022**, *188*, 114445.

(15) Dongsar, T. T.; Dongsar, T. S.; Gupta, N.; Almalki, W. H.; Sahebkar, A.; Kesharwani, P. Emerging potential of 5-Fluorouracil-loaded chitosan nanoparticles in cancer therapy. *Journal of Drug Delivery Science and Technology* **2023**, *82*, 104371.

(16) Melim, C.; Magalhães, M.; Santos, A. C.; Campos, E. J.; Cabral, C. Nanoparticles as phytochemical carriers for cancer treatment: News of the last decade. *Expert Opinion on Drug Delivery* **2022**, *19* (2), 179−197.

(17) Dey, D. K.; Sharma, C.; Vadlamudi, Y.; Kang, S. C. CopA3 peptide inhibits MDM2-p53 complex stability in colorectal cancers and activates p53 mediated cell death machinery. *Life Sci.* **2023**, *318*, 121476.

(18) Balusamy, S. R.; Perumalsamy, H.; Huq, M. A.; Yoon, T. H.; Mijakovic, I.; Thangavelu, L.; Yang, D. C.; Rahimi, S. A comprehensive and systemic review of ginseng-based nanomaterials: Synthesis, targeted delivery, and biomedical applications. *Med. Res. Rev.* **2023**, *43* (5), 1374−1410.

(19) Zhang, J.; Li, J.; Shi, Z.; Yang, Y.; Xie, X.; Lee, S. M.; Wang, Y.; Leong, K. W.; Chen, M. pH-sensitive polymeric nanoparticles for co-delivery of doxorubicin and curcumin to treat cancer via enhanced pro-apoptotic and anti-angiogenic activities. *Acta Biomater* **2017**, *58*, 349−364.

(20) Wang, F.; Wang, Y.-C.; Dou, S.; Xiong, M.-H.; Sun, T.-M.; Wang, J. Doxorubicin-tethered responsive gold nanoparticles facilitate intracellular drug delivery for overcoming multidrug resistance in cancer cells. *ACS Nano* **2011**, *5* (5), 3679−3692.

(21) Zhang, J.; Lin, W.; Yang, L.; Zhang, A.; Zhang, Y.; Liu, J.; Liu, J. Injectable and pH-responsive self-assembled peptide hydrogel for promoted tumor cell uptake and enhanced cancer chemotherapy. *Biomaterials Science* **2022**, *10* (3), 854−862.

(22) Solovieva, M.; Shatalin, Y.; Odinokova, I.; Krestinina, O.; Baburina, Y.; Mishukov, A.; Lomovskaya, Y.; Pavlik, L.; Mikheeva, I.; Holmuhamedov, E.; et al. Disulfiram oxy-derivatives induce entosis or paraptosis-like death in breast cancer MCF-7 cells depending on the duration of treatment. *Biochim Biophys Acta Gen Subj* **2022**, *1866* (9), 130184.

(23) Kim, Y.-J.; Perumalsamy, H.; Markus, J.; Balusamy, S. R.; Wang, C.; Ho Kang, S.; Lee, S.; Park, S. Y.; Kim, S.; Castro-Aceituno, V.; et al. Development of Lactobacillus kimchicus DCY51T-mediated gold nanoparticles for delivery of ginsenoside compound K: in vitro photothermal effects and apoptosis detection in cancer cells. *Artificial Cells, Nanomedicine, and Biotechnology* **2019**, *47* (1), 30−44.

(24) Lee, J. H.; Kim, I. W.; Kim, S. H.; Yun, E. Y.; Nam, S. H.; Ahn, M. Y.; Kang, D. C.; Hwang, J. S. Anticancer activity of CopA3 dimer peptide in human gastric cancer cells. *BMB Rep* **2015**, *48* (6), 324−329.

(25) Sharma, A.; Lee, H. J. Ginsenoside Compound K: Insights into Recent Studies on Pharmacokinetics and Health-Promoting Activities. *Biomolecules* **2020**, *10* (7), 1028.

(26) Mallick, A.; More, P.; Ghosh, S.; Chippalkatti, R.; Chopade, B. A.; Lahiri, M.; Basu, S. Dual drug conjugated nanoparticle for simultaneous targeting of mitochondria and nucleus in cancer cells. *ACS Appl. Mater. Interfaces* **2015**, *7* (14), 7584−7598.

(27) Akrami, M.; Balalaie, S.; Hosseinkhani, S.; Alipour, M.; Salehi, F.; Bahador, A.; Haririan, I. Tuning the anticancer activity of a novel pro-apoptotic peptide using gold nanoparticle platforms. *Sci. Rep* **2016**, *6*, 31030.

(28) Ocansey, D. K. W.; Yuan, J.; Wei, Z.; Mao, F.; Zhang, Z. Role of ferroptosis in the pathogenesis and as a therapeutic target of inflammatory bowel disease (Review). *Int. J. Mol. Med.* **2023**, *51* (6), 53.

(29) Wang, D.; Tang, L.; Zhang, Y.; Ge, G.; Jiang, X.; Mo, Y.; Wu, P.; Deng, X.; Li, L.; Zuo, S.; et al. Regulatory pathways and drugs associated with ferroptosis in tumors. *Cell Death Dis* **2022**, *13* (6), 544.

(30) Bouback, T. A.; Pokhrel, S.; Albeshri, A.; Aljohani, A. M.; Samad, A.; Alam, R.; Hossen, M. S.; Al-Ghamdi, K.; Talukder, M. E. K.; Ahammad, F. Pharmacophore-Based Virtual Screening, Quantum Mechanics Calculations, and Molecular Dynamics Simulation Approaches Identified Potential Natural Antiviral Drug Candidates against MERS-CoV S1-NTD. *Molecules* **2021**, *26* (16), 4961.

(31) Bharadwaj, S.; Dubey, A.; Yadava, U.; Mishra, S. K.; Kang, S. G.; Dwivedi, V. D. Exploration of natural compounds with anti-SARS-CoV-2 activity via inhibition of SARS-CoV-2 Mpro. *Brief Bioinform* **2021**, *22* (2), 1361−1377.

(32) Samad, A.; Huq, M. A.; Rahman, M. S. Bioinformatics approaches identified dasatinib and bortezomib inhibit the activity of MCM7 protein as a potential treatment against human cancer. *Sci. Rep* **2022**, *12* (1), 1539.

(33) Zhao, Y.; Zhao, W.; Lim, Y. C.; Liu, T. Salinomycin-Loaded Gold Nanoparticles for Treating Cancer Stem Cells by Ferroptosis-Induced Cell Death. *Mol. Pharmaceutics* **2019**, *16* (6), 2532−2539.

(34) Yadav, M.; Niveria, K.; Sen, T.; Roy, I.; Verma, A. K. Targeting nonapoptotic pathways with functionalized nanoparticles for cancer therapy: current and future perspectives. *Nanomedicine (London, England)* **2021**, *16* (12), 1049−1065.

(35) Wu, W.; Geng, Z.; Bai, H.; Liu, T.; Zhang, B. Ammonium Ferric Citrate induced Ferroptosis in Non-Small-Cell Lung Carcinoma through the inhibition of GPX4-GSS/GSR-GGT axis activity. *Int. J. Med. Sci.* **2021**, *18* (8), 1899−1909.

(36) Liu, Y.; Perumalsamy, H.; Kang, C. H.; Kim, S. H.; Hwang, J.-S.; Koh, S.-C.; Yi, T.-H.; Kim, Y.-J. Intracellular synthesis of gold nanoparticles by Gluconacetobacter liquefaciens for delivery of peptide CopA3 and ginsenoside and anti-inflammatory effect on lipopolysaccharide-activated macrophages. *Artificial Cells, Nanomedicine, and Biotechnology* **2020**, *48* (1), 777−788.